Synthetic Aptamer Mechanoreceptors Enable Cell-Specific Force Sensing and Temporal Control via DNA Circuits

Tao Xu[1], Soumya Sethi[1], Christoph Drees[1], and Andreas Walther[1,2]*

Affiliations

[1] Life-Like Materials and Systems, University of Mainz, Duesbergweg 10-14, Mainz 55128, Germany.

[2] Max Planck Institute for Polymer Research, Ackermannweg 10, 55128 Mainz, Germany.

*Corresponding author. Email: andreas.walther@uni-mainz.de

Abstract

Cells interpret mechanical cues from their microenvironment with spatiotemporal precision to guide adaptive behaviors. However, engineering synthetic mechanosensing systems with both cell-specificity and programmability remains challenging, especially when targeting ubiquitous classical mechanoreceptors. Here, we introduce an all-DNA mechanosensing platform based on aptamers that transmit force through noncanonical surface receptors. Aptamer–receptor recognition acts as a molecular gate for force transduction, enabling the design of mechanoprobes with dual selectivity – by force magnitude and cell type. These probes interpret diverse mechanical inputs via distinct mechanisms, including actomyosin-driven contractility relayed through focal adhesions and membrane ruffling during macropinocytosis. By integrating aptamer mechanoprobes with upstream DNA reaction networks, we achieve reversible and temporally programmable mechanoresponses. This modular, all-nucleic-acid system offers a general framework for constructing tunable mechanotransduction circuits. It expands the design space for synthetic mechanobiology and provides new opportunities for autonomous, multi-layered mechanical–biochemical regulation in tissue engineering, morphogenesis, and dynamic cell programming.

Introduction

Mechanical forces are key regulators of cellular behavior, shaping processes from morphogenesis to disease progression by guiding how cells sense, adapt, and respond to their microenvironment.[1–4] These responses are typically mediated by mechanoreceptors, which transduce physical stimuli into biochemical signals controlling cell fate, tissue structure, and homeostasis. Understanding and customizing the mechanotransduction process is pivotal for advancing mechanotargeting-based therapies, tissue engineering, and regenerative medicine.[5,6] However, orchestrating orthogonal cell-specific processes and implementing autonomous control mechanisms during complex morphogenesis is still challenged by the limited specificity, versatility, and dynamic tunability of the current mechanosensing toolbox.[7–9]

Selectivity and differential force sensing at the cellular level are key design principles for engineering synthetic mechanosensing materials. Cells endogenously express a variety of mechanoreceptors including integrins, cadherins, T cell receptors, and Piezo channels to accommodate diverse mechanical demands.[10–13] To engage with those, integrin-targeting mechanoprobes (MPs) have been most widely explored.[14] Pioneering studies have employed DNA-based MPs with Arg-Gly-Asp (RGD) motifs to measure piconewton (pN) forces transmitted through integrins. Depending on the DNA architecture, such probes can provide either irreversible ("historical") readouts via duplex rupture or reversible ("real-time") readouts via hairpin unfolding.[15] Recent innovations have even enabled quantification of single-molecule force loading rates.[16,17] However, the broad and often non-specific expression of integrins across cell types undermines terminal specificity[10,18], limiting their applicability in mixed or heterogeneous cell populations. Greater selectivity can be achieved using protein- or antibody-based ligands conjugated to DNA-MPs, which have proven valuable for interrogating T cell signaling and for constructing mechanosensitive cel-cell junctions.[12,19] In addition to sensing forces, previous DNA MPs have made use of force-induced strand separation to reveal cryptic domains amenable for downstream reactivity, such as in situ dimerization or for ex situ amplification.[20,21] Fully protein-based sensors that mimic Notch signaling offer additional strategies to encode both receptor specificity and force responsiveness, yet these approaches typically require labor-intensive protein engineering, including insertion-site optimization to maintain receptor localization and biological function – thereby limiting accessibility, modularity, and scalability.[22,23]

We hypothesized that aptamers – short single-stranded DNA sequences (ssDNA) selected for high-affinity binding to specific cell surface receptors – could serve as a versatile and new family of synthetic mechanosensors. Unlike classical mechanotransduction targets such as integrins or cadherins, many aptamer-accessible receptors are not canonically associated with force transmission. However, given their roles in signaling, trafficking, and cell migration, and since cells continuously recycle surface proteins for quality control, these receptors may transiently interact with the cytoskeleton or become indirectly coupled to intracellular

force-generating machinery – potentially enabling mechanical engagement through previously unrecognized mechanisms. Indeed, a recent proof-of-concept using the CI-M6PR aptamer demonstrated that even weak endocytic forces (~4 pN[24]) can be sensed using a DNA MP.[20] However, that system required soft DNA hairpins suffering from dynamic breathing behavior, which limits force resolution and complicates integration with DNA reaction circuits. More generally, the design space for aptamer-based force sensors remains largely unclear – particularly in terms of cell-type specificity, force thresholding, and mechanistic understanding of how force is generated at the aptamer-receptor interface. Importantly, because aptamers are nucleic acids, they are inherently compatible with DNA-based strand displacement reactions and programmable logic circuits.[25–27] This opens opportunities for dynamic and autonomous regulation of mechanosensing – features that are difficult to achieve with conventional peptide- or protein-based systems like RGD-integrin probes or SynNotch receptors.

Here, we present a modular and fully programmable mechanosensing platform built entirely from nucleic acids, in which DNA aptamers function as synthetic receptor ligands embedded within force-responsive DNA MPs. This approach combines the receptor specificity of aptamers with the tunable force thresholds of DNA mechanics, enabling the systematic exploration of non-canonical and previously unrecognized force-generating surface receptors across diverse cell types. Using this platform, we demonstrate two key modes of selectivity: cell-type selectivity, dictated by aptamer-receptor binding; and force selectivity, governed by DNA MP geometry and loading direction. In contrast to conventional integrin-targeting RGD probes, our aptamer MPs display distinct force transmission behaviors, revealing new mechanistic insights into how specific receptor contexts modulate mechanical engagement. Going further, leveraging the nucleic acid nature of aptamers, we integrate these probes with upstream DNA-based reaction networks to achieve temporal gating and switchable mechanosensitivity. This platform establishes a general framework for constructing adaptive, programmable mechano-interfaces and expands the synthetic biology toolkit for force-guided cell control.

Results

General concept for aptamer-based mechanosensing platform

Our aptamer-based MPs are composed of three modular elements: a terminal aptamer that selectively binds a target receptor, a DNA duplex that acts as a tunable force-sensitive element, and a fluorophore–quencher pair that converts mechanical unfolding into a fluorescence signal (**Fig. 1**). The aptamer functions as a programmable ligand, enabling receptor-specific engagement and ensuring that only receptor-expressing cells generate detectable force signals. To demonstrate the versatility of this platform, we employ five distinct and frequently used aptamers targeting diverse cell-surface receptors across five different cell lines. Moreover, the nucleic acid-based architecture of the aptamer permits dynamic control of receptor recognition via complementary blocker strands, which can be regulated through DNA-based reaction networks to achieve

multi-layered regulatory complexity, such as temporally gated mechanosensing. For surface functionalization, we immobilized biotinylated MPs onto streptavidin-coated glass slides and co-immobilized biotinylated RGD peptides in a 1:1 ratio to support integrin-mediated cell adhesion independent of the aptamer-receptor interaction.

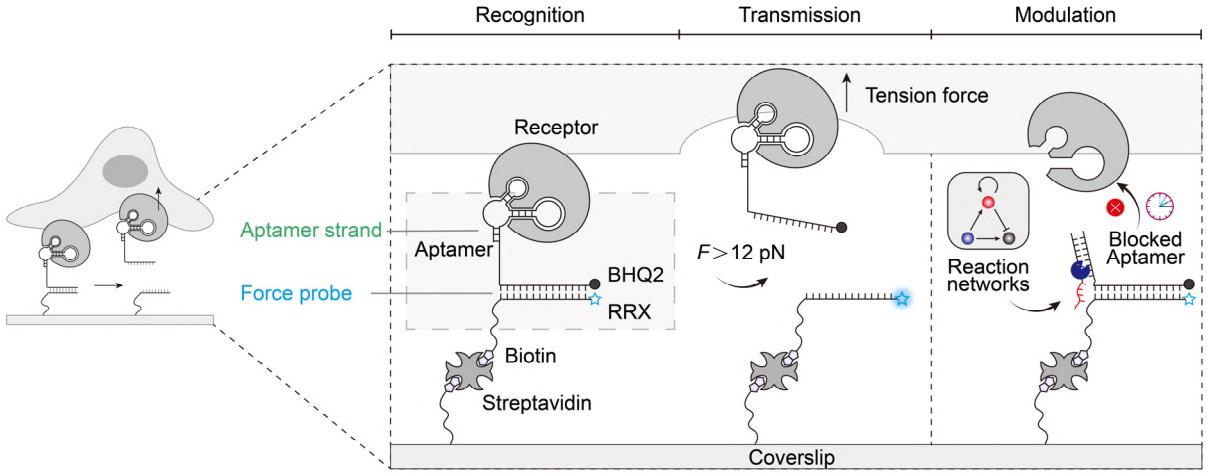

Fig. 1 Aptamer-based mechanoprobes (MPs) enable cell-type-specific mechanosensing and programmable control via upstream DNA reaction networks. The all-nucleic-acid MP consists of a cell-targeting aptamer ligand and a DNA duplex serving as a force sensor. A fluorophore–quencher pair (Rhodamine Red X and BHQ2) transduces mechanical forces into fluorescence signals upon duplex dissociation. Specific force transmission is gated by aptamer–receptor recognition, allowing for cell-type-selective responses. Tuning the geometry of the duplex enables force thresholding to filter defined mechanical inputs. Integration with upstream DNA reaction networks (DRNs) permits programmable and nonlinear regulation of aptamer accessibility, establishing a versatile framework for engineered mechanotransduction.

Force transmission of aptamer MP requires specific aptamer-receptor recognition

To investigate the role of aptamer–receptor recognition in mechanosensing, we designed a MP incorporating the AS1411 aptamer, which binds nucleolin (dissociation constant K_d = 69.1 nM)[28] – a membrane-associated receptor overexpressed in many cancer cells.[29] We selected nucleolin-rich HeLa cells as the test system and used an AS1411 MP with a zipper-type duplex designed to rupture under a low force tolerance (T_{tol}) of 12 pN. Subsequently, we seeded cells onto the MP-functionalized surface and imaged them by total internal reflection fluorescence (TIRF) microscopy after 4 h incubation at 37 °C in 1 % FBS/DMEM medium. Two controls highlight the successful specific activation: One control bears a randomized sequence without affinity to nucleolin, and one lacks any ligand (**Fig. 2**a). As expected, only the AS1411 MP generates significant fluorescence, confirming that specific aptamer-receptor binding enables force transmission (**Fig. 2**a,b). Neither control produces signal, confirming the absence of any nonspecific interactions, such as from dye-membrane interactions (**Fig. 2**b). Interestingly, cell spreading area and cell aspect ratio are similar for the three surfaces (AS1411 MP, random MP and negative control) within the 4 h observation period, indicating that the AS1411-nucleolin couple operates independently of RGD-integrin mediated adhesion (**Fig. 2**c, Supplementary Fig. 1).

Next, we validate that the AS1411 MP specifically engages the nucleolin receptor by performing colocalization and competitive binding assays. To this end, we employed the TB-5 aptamer, which binds to a distinct epitope on nucleolin compared to AS1411, and co-immobilized TB-5[30] and AS1411 MP on the surface at a 1:1 ratio. The mechanosignals from both MPs colocalize, confirming that they both engage nucleolin (**Fig. 2**d). To further confirm specificity, we blocked the AS1411–nucleolin interaction using endostatin, a natural ligand for nucleolin,[29] which reduces the AS1411-derived mechanosignals by 21.7% (**Fig. 2**e). Flow cytometry corroborates this finding, showing a 23.2% decrease in AS1411 binding to HeLa cells in the presence of endostatin (Supplementary Fig. 2). Together, these results demonstrate that force transmission through the AS1411 MP originates from specific aptamer–receptor recognition.

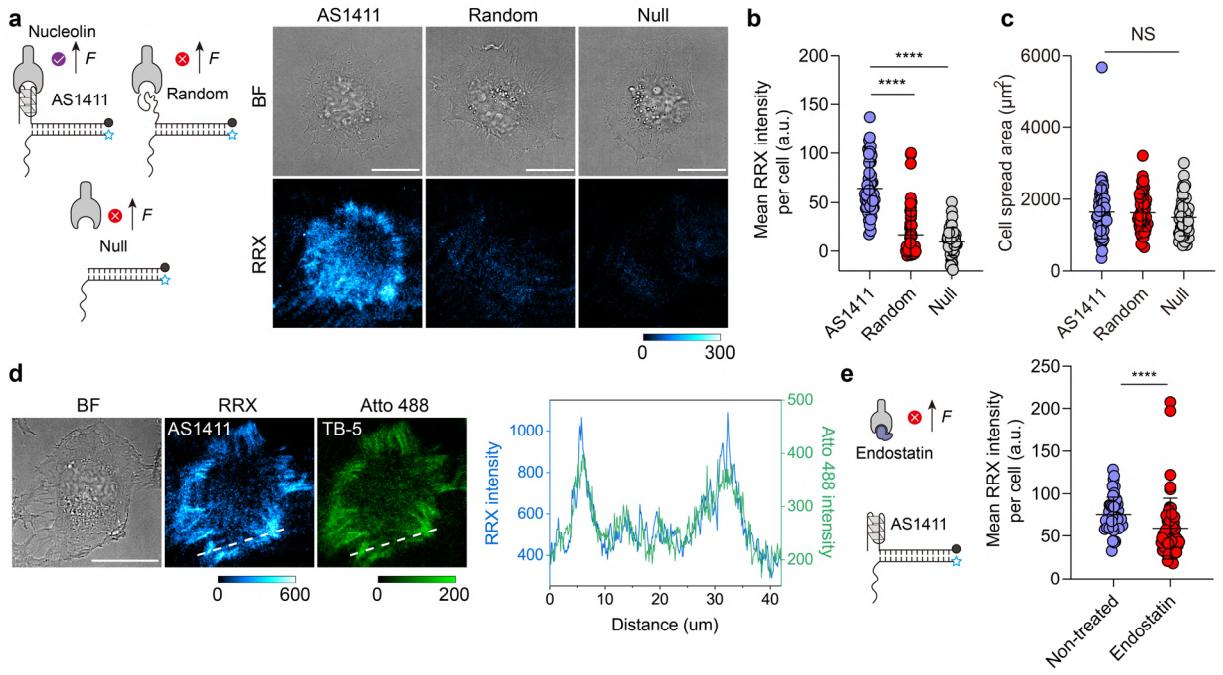

Fig. 2 Specific aptamer–receptor recognition is required for mechanosensing by aptamer-based MPs. a Schematic and representative TIRF images of HeLa cells cultured on surfaces functionalized with AS1411 aptamer, a randomized sequence, or no ligand. **b-c** Quantification of mean fluorescence intensity per cell (**b**) and cell spreading area (**c**) for HeLa cells on each surface. *n* = 54 cells from 3 replicates. **d** Representative brightfield and fluorescence images (TIRF mode) of HeLa cells cultured on surfaces functionalized with a 1:1 ratio of AS1411 and TB-5 MPs. Line profile shows colocalization of AS1411 and TB-5 mechanosignals. **e** Scheme and quantification of mean fluorescence intensity per cell of HeLa cells without and with endostatin blocking (25 μg/mL) on AS1411 MP surfaces. *n* = 45 (control), 54 (blocked) cells from 3 replicates. Statistics (b, c): Kruskal-Wallis test with Dunn's multiple comparisons, (e) Two-tailed, Mann-Whitney test. Scale bars = 20 μm.

Aptamer MP exhibits enhanced force selectivity

To compare the force sensitivity of AS1411 MPs with commonly used RGD-based MPs,[21] we designed each with two distinct force geometries. In the unzipping mode, the duplex opens base-by-base, resulting in a low T_{tol} of 12 pN. In contrast, the shearing mode applies force across multiple base pairs near the duplex termini, yielding a higher T_{tol} of 54 pN based on sequence design (**Fig. 3**a).[15]

Comparing first both RGD MPs, the RGD-unzipping MP produces markedly stronger fluorescence signals than the RGD-shearing MP, particularly at peripheral focal adhesions (FAs) and at central regions indicative of early-stage adhesion events (**Fig. 3**b). This pattern reflects the lower T_{tol} of the unzipping mode, which enables detection of nascent, low-force adhesion events that fail to activate RGD-shearing MP. Although altering the force geometry modulates the average mechanoresponse pattern per cell (**Fig. 3**c), the overall response based on the integrated intensity remains indistinguishable and independent of the MP geometry (**Fig. 3**d). This apparent convergence arises because RGD-integrin linkages are capable of transmitting single-molecule forces that exceed both T_{tol} values (>54 pN), and in some cases can even rupture the streptavidin-biotin linkage (> 100 pN).[31] However, the generation of such high forces is contingent on adequate mechanical resistance from the substrate – typically requiring 33-44 pN counterforce to sustain cytoskeletal maturation and stable adhesion.[32] As a result, shearing-mode MPs promote cell spreading and increase overall force generation, thereby blurring the difference in integrated mechanoresponse between both geometries (**Fig. 3**e).[19]

In contrast, AS1411 MPs show a pronounced distinction between unzipping and shearing geometry. The unzipping mode consistently produces stronger signals in both mean and integrated intensity (**Fig. 3**b-d). Two factors account for this behavior: First, the AS1411-nucleolin couple transmits substantially lower force than RGD-integrin engagement. Second, unlike integrins, the AS1411-nucleolin pair alone does not promote cell spreading (**Fig. 2**c, and **Fig. 3**e). As a result, AS1411 MPs exhibit enhanced force selectivity, with minimal cross activation between geometries. This property makes the shearing mode particularly well-suited for tandem integration with other DNA nanodevices,[33,34] where mechanical stability is essential to avoid unintended force-induced detachment.

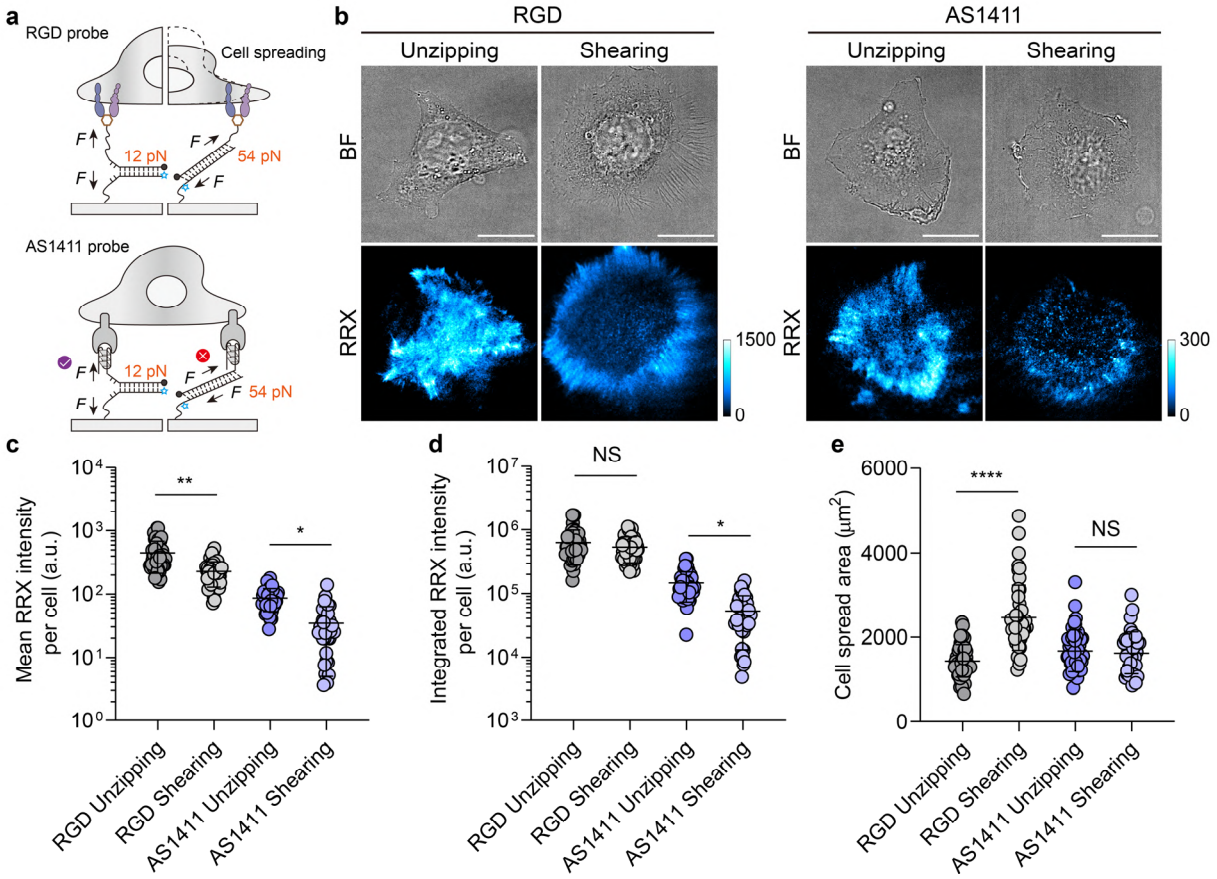

Fig. 3 Aptamer MPs enable force selectivity via distinct duplex geometries. a Scheme of the mechanosensing through unzipping and shearing geometries in RGD and AS1411 MPs. **b** Representative brightfield and fluorescence images of HeLa cells cultured on surfaces functionalized with RGD and AS1411 MPs featuring different force geometries. **c-e** Quantification of (**c**) mean fluorescence intensity per cell, (**d**) integrated fluorescence intensity per cell, and (**e**) cell spreading area for HeLa cells on each MP type and geometry. *n* = 49, 47, 45, 36 (left to right) cells from 3 replicates. Statistics: Kruskal-Wallis test with Dunn's multiple comparisons. Scale bars = 20 µm

Source of forces associated with noncanonical mechanoreceptors

Although nucleolin is a well-established molecular target,[35,36] it has not been previously associated with the exertion of mechanical force on the extracellular environment. Our data reveal distinct differences to integrin-targeting MPs, prompting us to investigate the source of nucleolin-associated forces. To test whether aptamer-receptor internalization contributes to force generation, we treated HeLa cells with pathway-specific inhibitors. Neither chlorpromazine (CPZ, 28 µM), which inhibits clathrin-mediated internalization,[37] nor methyl-β-cyclodextrin (MβCD, 1.9 µM) which inhibits caveolin- and lipid-raft-mediated uptake,[38] alters the mechanosignal intensity (**Fig. 4**a, b). In contrast, treatment with 5-(N-ethyl-N-isopropyl) amiloride (EIPA, 100 µM), an inhibitor of macropinocytosis,[39] reduces mechanosignals by 29.8 % (**Fig. 4**b). This implicates macropinocytosis in the mechanoactivation of the AS1411 MP, consistent with previous findings that cancer cells take up free AS1411 aptamers predominantly via macropinocytosis.[40] Flow cytometry further supports this conclusion, showing a 76.6 % reduction in the uptake of free AS1411 aptamers by HeLa cells in the presence of EIPA (Supplementary Fig. 3). Notably, compared to the free state in solution, the inhibitory effect

177 of EIPA decreases by 46 % when AS1411 is immobilized as a MP on a surface. These results suggest that while
178 macropinocytosis contributes to force generation, it may not be the main source of nucleolin-mediated force.

179 Interestingly, previous studies reported molecular associations between nucleolin and FA proteins such as
180 talin.[41] To determine whether nucleolin-mediated forces spatially correlate with FA structures, we transfected
181 HeLa cells with a plasmid for constitutive expression of monomeric enhanced green fluorescent protein
182 (mEGFP)-paxillin and visualized the actin cytoskeleton with phalloidin staining. Notably, nucleolin-generated
183 forces are clearly localized at peripheral FA sites marked by paxillin, suggesting a spatial and functional
184 association between nucleolin and FAs (**Fig. 4**c, d, Supplementary Fig. 4). Based on this, we hypothesized
185 nucleolin may indirectly couple to the actomyosin cytoskeleton to transmit mechanical force
186 (**Fig. 4**e). To identify the cytoskeletal components responsible for this transmission, we treated cells with
187 specific inhibitors after allowing 30 min of initial adhesion.[16,42] Inhibiting actin polymerization with cytochalasin
188 D (10 μM) moderately reduces mechanosignals by 38.9 % (**Fig. 4**f, Supplementary Fig. 5). In contrast, blocking
189 myosin II ATPase activity with blebbistatin (25 μM) causes a pronounced 77.5 % decrease. Together, these
190 results demonstrate that nucleolin-mediated forces primarily depend on myosin-driven contractility, which
191 may be relayed through FAs before reaching nucleolin.

192 Considering that we aim to develop receptor-orthogonal aptamer MPs, we further investigated the Sgc8-
193 aptamer as a potential MP for the protein tyrosine kinase 7 (PTK7), using HepG2 cells that overexpress this
194 receptor. Similar to the nucloelin system, the Sgc8-unzipping MP with a T_{tol} of 12 pN generates strong
195 mechanosignals (**Fig. 4**g). However, unlike the FA-like patterns observed for nucleolin, PTK7-activated
196 mechanosignals display spatially distinct, ring-like force patterns with submicron size (**Fig. 4**g). Those are
197 consistent with a macropinocytic origin, as clathrin- and caveolin-mediated internalization typically generates
198 vesicles in the nanometer range.[43] To test this hypothesis, we inhibited macropinocytosis using EIPA (100 μM),
199 which substantially reduces mechanoactivation by 51.9 %, whereas CPZ (28 μM) and MβCD (1.9 μM) inhibiting
200 clathrin- and caveolin-mediated endocytosis have no effect (**Fig. 4**g, h, Supplementary Fig. 6). To further
201 examine the spatial organization of these signals, we stained the plasma membrane and performed TIRF
202 microscopy. As expected, the ring-like mechanofluorescence predominantly localizes to the peripheries of dark
203 membrane invaginations, consistent with force generation during membrane ruffling in early-stage
204 macropinocytosis (**Fig. 4**i, j, Supplementary Fig. 7).[44]

205 To understand the cytoskeletal origin of this force generation, we next examined the roles of actin
206 polymerization and myosin action during different macropinocytic phases. Actin polymerization is critical for
207 driving membrane ruffling and protrusion formation during the early-stage macropinocytosis, whereas
208 myosins contribute to actin network contraction at the base of ruffles as the membrane closes to form
209 macropinosomes.[45] Treatment with cytochalasin D (10 μM, actin polymerization inhibitor) and blebbistatin (25

210 μM, myosin II inhibitor) reduces mechanosignals by 56.1 % and 32.6 %, respectively, suggesting that force
211 generation is dominated by actin polymerization rather than myosin-driven contraction (**Fig. 4**k,
212 Supplementary Fig. 8). Phosphoinositide 3-kinase (PI3K) catalyzes membrane sealing by generating PIP_3 at the
213 ruffle bases, thereby recruiting effectors for actin remodeling and vesicle closure.[46] While PI3K activity is
214 essential for membrane sealing, it is dispensable for ruffle formation.[47] Consistent with this, inhibition of PI3K
215 using LY294002 (50 μM) does not affect mechanosignals, further confirming that PTK7-mediated forces
216 originate primarily from early-stage membrane ruffling during macropinocytosis with minimal contribution
217 from the sealing phase (**Fig. 4**l,m).

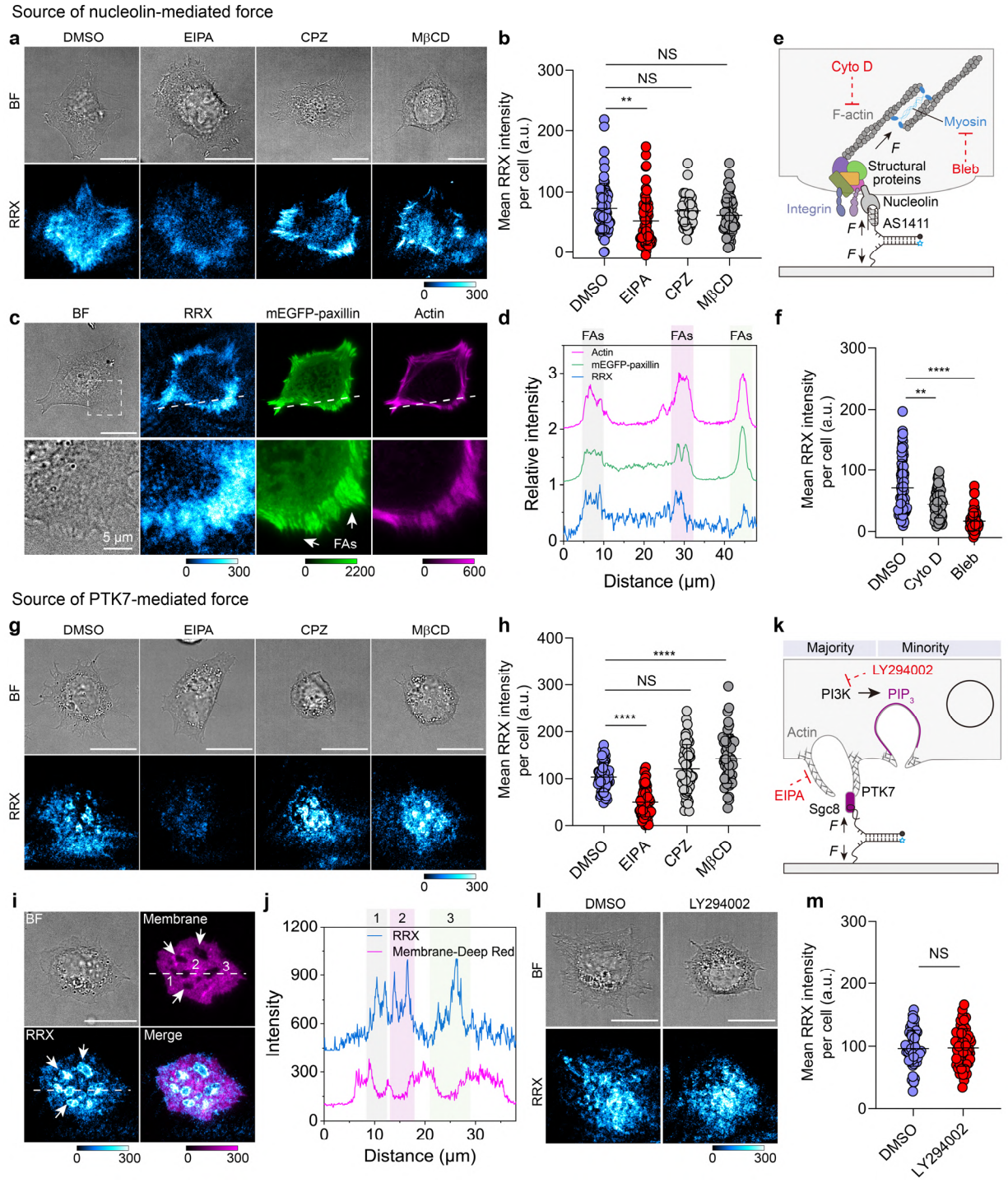

Fig. 4 Aptamer MPs reveal force origins associated with noncanonical mechanoreceptors. a Representative brightfield and fluorescence images of HeLa cells treated with internalization inhibitors on AS1411 MP surfaces. **b** Quantification of mean fluorescence intensity per cell for HeLa cells under the indicated conditions. *n* = 70, 70, 54, 54 (left to right) cells from 3 replicates. Statistics: Kruskal-Wallis test with Dunn's multiple comparisons. **c** Representative images of HeLa cells on AS1411 MP surfaces showing brightfield, mechanosignal, mEGFP-paxillin, and phalloidin-stained actin. **d** Line profile along the white line in (c) shows intensity profiles of mechanosignals, mEGFP-paxillin, and actin. **e** Schematic: forces acting on nucleolin arise from myosin-II-driven contractility transmitted via focal adhesions (FAs). **f** Quantification of mean fluorescence intensity per cell following cytoskeletal inhibitor treatment. *n* = 72 cells from 3 replicates. Statistics: Kruskal-Wallis test with Dunn's multiple comparisons. **g** Representative brightfield and fluorescent images of HepG2 cells treated with internalization inhibitors on Sgc8 MP surfaces. **h** Corresponding quantification of mean fluorescence

intensity per cell. *n* = 54 cells from 3 replicates. Statistics: One-way ANOVA with Bonferroni post-hoc tests. **i** Representative images showing plasma membrane staining, mechanosignals and brightfield of HepG2 cells incubated on Sgc8 MP surfaces. **j** Line profile from (i) reveals spatial colocalization of mechanosignals at the inner edge of membrane invaginations. **k** Schematic: PTK7-mediated forces originate from membrane ruffling during early-stage macropinocytosis; membrane sealing contributes minimally. **l** Brightfield and fluorescence images of HepG2 cells treated with PI3K inhibitor LY294002 on Sgc8 MP surfaces. **m** Quantification of mean fluorescence intensity per cell for HepG2 cells without and with LY294002 treatment on Sgc8 MP surfaces. *n* = 54 cells from 3 replicates. Statistics: Unpaired, two-tailed student's *t*-test. Scale bar = 20 µm.

Versatility of aptamer MPs to customize cell-type-specific mechanoresponses

The specificity of aptamer-receptor recognition enables the modular customization of MPs for cell-type-specific mechanosensing. We demonstrate this principle using three aptamer MPs – Sgc8, MUC1 S2.2 and SYL3c – which target PTK7 (K_d = 0.85 nM)[48], mucin-1 (K_d = 0.12 nM)[49], and epithelial cell adhesion molecule (EpCAM, K_d = 38 nM)[50], respectively. We tested each MP on both receptor-positive and receptor-negative cell lines, selected based on differential receptor expression profiles confirmed by flow cytometry (Supplementary Fig. 9). PTK7-positive HepG2 cells strongly activate the Sgc8 MP, whereas A549 cells with substantially lower levels of PTK7 show minimal response (**Fig. 5**a,b). Conversely, HepG2 cells fail to activate the MUC1 S2.2 probe due to low mucin-1 receptor levels. This contrasts with mucin-1-positive HeLa cells (**Fig. 5**c,d). Similarly, MDA-MB-231 cells generate stronger activation of the SYL3c probe than HeLa cells, consistent with their higher EpCAM expression (**Fig. 5**e,f). These results collectively demonstrate high differential selectivity of aptamer-receptor MP pairs and highlight the broad adaptability of our platform for sensing mechanoresponses across diverse cell types and receptor classes.

Motivated by the need for selective and precise mechanoresponse in complex multicellular environments, we extend our validation beyond simple single-cell-type systems. To this end, we labeled receptor-positive and receptor-negative cells with CellTrace Deep Red and Violet dyes, respectively, and co-seeded them in wells containing the corresponding aptamer MPs to assess cell-type-specific mechanoresponse (**Fig. 5**g). Indeed, mechanoactivation of the MUC1 S2.2 MP occurs exclusively in the Deep Red-labeled mucin-1-positive HeLa cells, while the Violet-labeled Mucin-1-negative HepG2 cells exhibit much lower signals (**Fig. 5**h,i). Switching to the Sgc8 MP leads to strong mechanosignals in the Deep Red-labeled PTK7-positive HepG2 cells, whereas Violet-labeled PTK7-negative A549 cells show minimal signals (**Fig. 5**j,k). These results underscore the utility of aptamer MPs as customizable mechanical elements for precise, cell-type-specific mechanochemical transduction in heterogeneous cell populations.

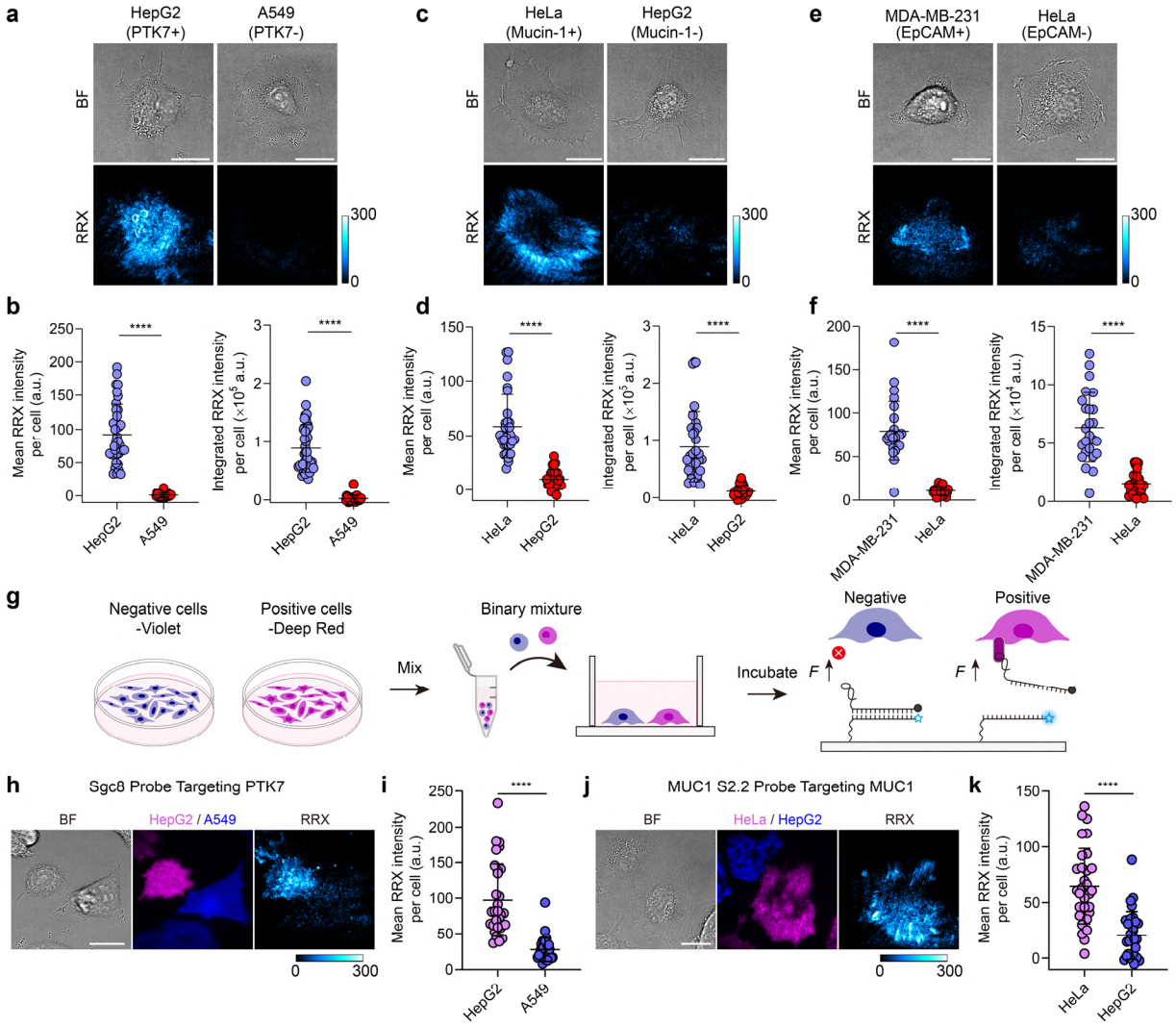

Fig. 5 Customized cell-type-specific mechanoactivation enabled by aptamer-receptor recognition. a Representative brightfield and fluorescence images of HepG2 (PTK7-positive) and A549 (PTK7-negative) cells on Sgc8 MP surfaces. **b** Corresponding quantification of mean and integrated fluorescence intensity per cell of HepG2 and A549 cells on Sgc8 MP surfaces. *n* = 36, 27 cells from 3 replicates. Statistics: Two-tailed, Mann-Whitney test. **c** Representative images of HeLa (mucin-1-positive) and HepG2 (mucin-1-negative) cells on MUC1 S2.2 MP surfaces. **d** Corresponding quantification of mean and integrated fluorescence intensity per cell of HeLa and HepG2 cells on MUC1 S2.2 MP surfaces. *n* = 31, 27 cells from 3 replicates. Statistics: Two-tailed, Mann-Whitney test. **e** Representative images of MDA-MB-231 (EpCAM-positive) and HeLa (EpCAM-negative) cells on SYL3c MP surfaces. **f** Corresponding quantification of mean and integrated fluorescence intensity per cell of MDA-MB-231 and HeLa cells on SYL3c MP surfaces. *n* = 25, 27 cells from 3 replicates. Statistics: Two-tailed, Mann-Whitney test. **g** Schematic of co-culture assay design. Receptor-positive and -negative cells were pre-labeled with CellTrace Deep Red and Violet dyes, respectively, mixed 1:1, and co-seeded onto aptamer MP-functionalized surfaces. **h** Representative images of HepG2 (PTK7-positive, Deep Red) and A549 (PTK7-negative, Violet) cells co-cultured on Sgc8 MP surfaces. **i** Quantification of mechanosignals in HepG2 vs A549 cells. n = 31 cells from 3 replicates. Statistics: Two-tailed, Mann-Whitney test. **j** Representative images of co-cultured HeLa (mucin-1-positive, Deep Red) and HepG2 (mucin-1-negative, Violet) cells on MUC1 S2.2 MP surfaces. **k** Corresponding quantification of mechanosignals as mean fluorescence intensity per cell. *n* = 31 cells from 3 replicates. Statistics: Unpaired, two-tailed student's *t*-test. Scale bars = 20 µm.

274 **Aptamer MPs enable programmable mechanoresponses via integration with DNA-based reaction networks**
275 **(DRNs)**

276 Natural mechanotransduction involves temporally orchestrated biochemical signals that guide adaptive
277 cellular responses. Aptamers, unlike protein or peptide ligands, offer the unique advantage that their DNA
278 structure can be seamlessly integrated with DRNs to emulate this dynamic regulation. Importantly, aptamers
279 can be manipulated directly at their binding site with DRNs without detaching them from the underlying
280 surface by for instance breaking the force-sensitive duplex, thus ensuring their correct configuration and
281 integrity.

282 To introduce temporal control over mechanoactivation, we regulate aptamer accessibility using designer
283 blocker and activator strands that can be designed with tunable affinities based on base-pairing principles (**Fig.**
284 **6**a). We first use a blocker fully complementary to AS1411 to completely prevent binding to nucleolin. This
285 blocker also contains a 5-nucleotide (nt) toehold, enabling its subsequent removal via a toehold-mediated
286 strand displacement reaction (SDR) triggered by an activator strand. In this design, mechanoactivation
287 becomes conditional on the possibility for aptamer-receptor engagement, which can be dynamically regulated
288 through SDR. Cell-free surface assays confirm robust and reversible aptamer blocking (Supplementary Fig. 10).
289 The blocker quenches >90 % of a fluorescently labeled, surface-tethered AS1411 aptamer within 30 min,
290 indicating effective blocking. Subsequent medium exchange with the equimolar activator restores ~ 50 % of
291 the signal within 30 min, confirming aptamer reactivation (Supplementary Fig. 10). We next validate this
292 mechanism under live-cell conditions. Adding 200 nM blocker 30 min after seeding suppresses AS1411-
293 nucleolin mechanoactivation by 75.1 %. Subsequent medium exchange with 200 nM activator restores 82.5 %
294 of the original signal, consistent with aptamer re-engagement and functional recovery of mechanosensing
295 (**Fig. 6**b,c).

296 Going a step beyond external switching, we next introduce more advanced enzyme-catalyzed DRNs upstream
297 of mechanoactivation to autonomously program the temporal accessibility of aptamer MPs.[26,27] To this end,
298 we replace the DNA blocker with an RNA analogue. This RNA blocker can be selectively degraded by RNase H
299 only when bonded as RNA-DNA duplex at the MP. This degradation releases the aptamer and restores
300 mechanoactivation within programmable time windows (**Fig. 6**d). In this context, RNase H acts as a biochemical
301 gatekeeper. Additional temporal control can be gained by introducing freely diffusing RNA-DNA duplexes as
302 decoy substrates, which compete with the RNA-blocked MP for RNase H activity.

303 The kinetics of the timer circuit for MP activation depend on the DRN parameters. First, the RNase H
304 concentration can be used to control the time for mechanoactivation to occur. Low RNase H concentrations
305 (≤1 U/ml) fail to initiate measurable mechanoresponse within 4 h. At 10 U/mL, mechanoactivation is restored
306 to 78.2%, while 100 U/mL yields near-complete recovery, consistent with efficient RNA blocker degradation

307 (**Fig. 6**e,f). To further tune the system, we then fixed RNase H at 10 U/mL and introduced the RNA-DNA decoy.
308 These indeed slows down the RNA blocker degradation (**Fig. 6**g). 10 nM of decoy is sufficient to modestly delay
309 the mechanoresponse, while 100 nM nearly abolishes the response within 4 h, with a significant increase
310 observed only at 7 h (**Fig. 6**h,i).

311 Because RNA-RNaseH modules can be extended into more complex signaling DRNs,[25] our aptamer
312 manipulation strategy opens doors for more complex temporal programs in the future. We note that similar
313 programmable mechanoactivation could also be achieved using antibody- or nanobody-based probes that
314 block receptor access via engineered protein blockers and activator with progressively tuned affinities.
315 However, such protein-based systems would require extensive efforts, including site-directed mutagenesis,
316 affinity optimization, and computational modeling to fine-tune the underlying protein–protein interactions. In
317 contrast, aptamer systems offer a far more accessible and modular alternative, leveraging predictable base-
318 pairing rules to design dynamic, multistage mechanical response circuits in a straightforward manner.

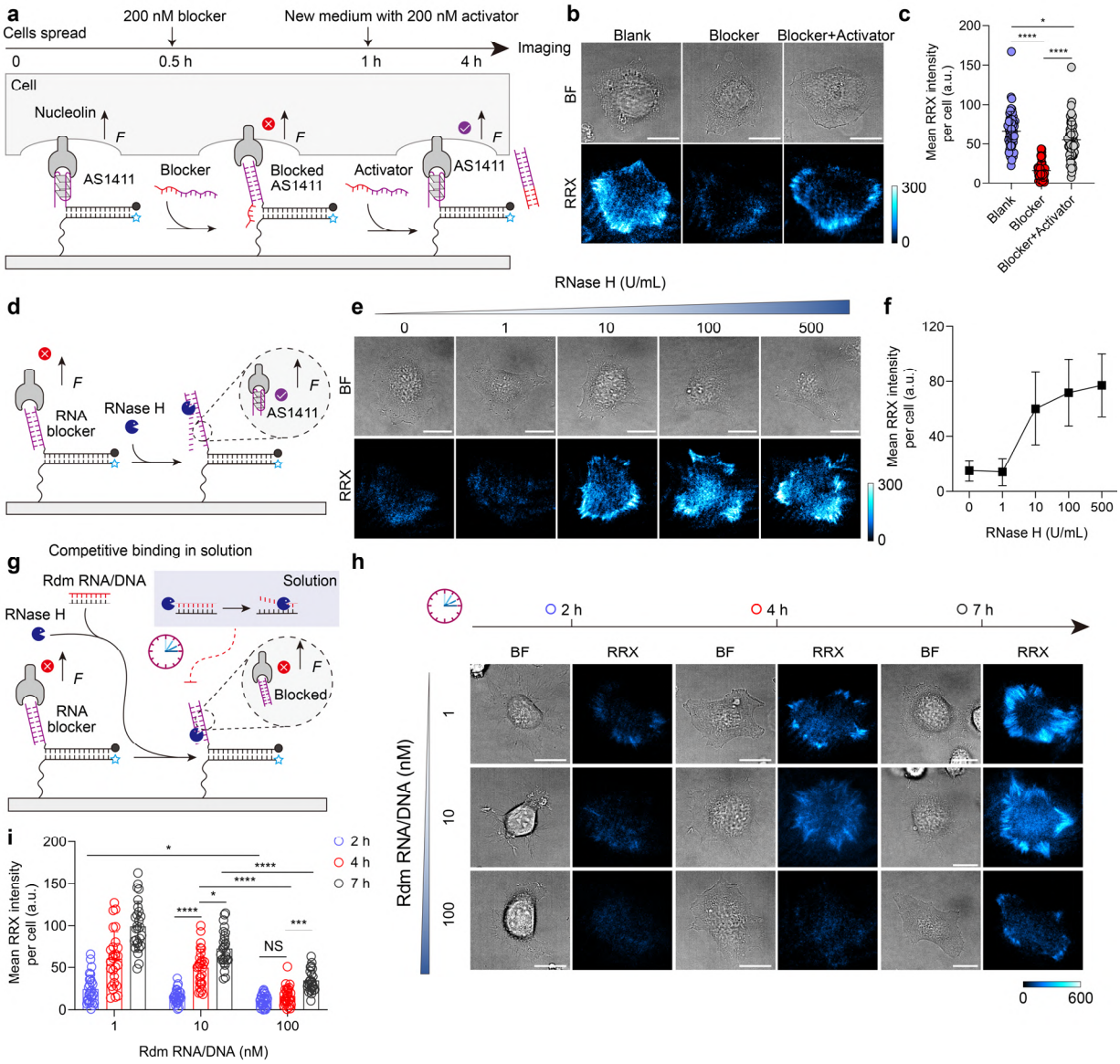

Fig. 6 Programmable mechanoactiovation enabled by upstream DRNs. a Schematic of switchable mechanosensing using SDRs. HeLa cells were seeded on surfaces grafted with AS1411 MP for 30 min, followed by addition of 200 nM DNA blocker strands to inhibit aptamer–receptor interaction. After another 30 min, 200 nM DNA activator strands were introduced to displace the blockers via toehold-mediated SDR, restoring mechanosensing. **b** Representative brightfield and fluorescence images of HeLa cells on AS1411 MP surfaces after sequential blocker and activator treatment. **c** Corresponding quantification of mean fluorescence intensity per cell. *n* = 54 cells from 3 replicates. Statistics: One-way ANOVA with Bonferroni post-hoc tests. **d** Schematic of enzyme-catalyzed mechanoactivation. Aptamer MPs are initially blocked by complementary RNA strands. Addition of RNase H at varying concentration (0-500 U/mL) degrades the RNA in the RNA–DNA duplexes, resetting the aptamer configuration and restoring mechanosensing. **e** Representative brightfield and fluorescence images of HeLa cells on RNA-blocked AS1411 MP surfaces following addition of different RNase H concentrations. **f** Corresponding quantification of mean fluorescence intensity per cell. *n* = 36 cells from 3 replicates. **g** Schematic of delayed mechanoactivation. Aptamer MPs are RNA-blocked and exposed to 10 U/mL RNase H. Increasing concentrations of freely diffusing RNA–DNA decoy duplexes (1–100 nM) compete for RNase H activity, thereby delaying aptamer reactivation. **h** Representative brightfield and fluorescence images of HeLa cells on RNA-blocked AS1411 MP surfaces after adding 10 U/mL RNase H and varying RNA/DNA duplex concentrations. **i** Corresponding quantification of mean fluorescence intensity per cell. Reaction medium: 1 % FBS, 1 % P/S, 100 µg/mL actin protein, DMEM. *n* = 27 cells from 3 replicates. Statistics: Two-way ANOVA with Geisser-Greenhouse correction followed by Bonferroni post-hoc tests. Scale bars = 20 µm.

336 **Conclusion**

337 We have introduced aptamer-based MPs as a specific, modular, and programmable platform for
338 mechanosensing that enables customizable mechanoresponses with dual selectivity – across both cell type
339 and force threshold. We find that aptamer–receptor recognition is a critical determinant of specific force
340 transmission. Exploiting distinct receptor expression profiles on different cells, it is now possible to engineer
341 cell-type-specific mechanoresponses that filter irrelevant mechanical stimuli and facilitate precise functional
342 specialization. Such capabilities are essential for constructing complex behaviors in multicellular systems.

343 To contextualize the advantages of aptamer MPs, it is instructive to compare them with conventional ligand–
344 receptor systems commonly used in mechanobiology. Although high-affinity ligands such as cRGDfK can
345 achieve targeted, force-responsive delivery of therapeutic agents (e.g., anticancer drugs or antisense
346 oligonucleotides) across $\alpha_v\beta_3$-positive cells,[34,51] their promiscuity toward various integrin subtypes and the
347 structural similarity among integrins limit specificity.[18] Moreover, RGD-integrin engagement promotes
348 adhesion reinforcement, which blurs discrimination between different force geometries. In contrast, aptamers,
349 as shown for the AS1411–nucleolin interaction, can be functionally decoupled from adhesion processes,
350 rendering the tension tolerance (T_{tol}) a dominant parameter in mechanoactivation. This enables the use of
351 aptamer MPs as force-selective mechanical gates and allows their modular integration with other DNA-based
352 nanodevices.

353 The excellent selectivity of aptamer MPs underscores their importance to interpret noncanonical
354 mechanoreceptors outside of the classical mechanobiology realm, enabling to decouple mechanoactivation
355 from intrinsic mechanotransduction pathways. On the molecular level, we have elucidated two distinct force
356 transmission behaviors: nucleolin-mediated forces arise from actomyosin contractility and are relayed via focal
357 adhesions, whereas PTK7-mediated forces originate from membrane ruffling during early-stage
358 macropinocytosis. These two cases are not meant to be exhaustive but rather exemplify that noncanonical
359 mechanoreceptors can engage in mechanical signaling via diverse, receptor-specific pathways. By proposing a
360 systematic framework for receptor-specific mechanosensing, we lay the groundwork for future exploration of
361 alternative mechanotransduction pathways. From a biological perspective, our findings raise intriguing
362 questions about the mechanical roles of nucleolin, PTK7, and other noncanonical mechanoreceptors. Whether
363 such receptors indirectly participate in other mechanotransduction pathways or contribute to extracellular
364 matrix remodeling remains to be elucidated. These newly uncovered mechanisms also contrast with aptamer
365 internalization by weak clathrin-based endocytic forces (~4 pN), which are limited to measurements with very
366 weak DNA hairpins.[20] In contrast, our aptamer MPs exert forces >12 pN, allowing for the exposure of cryptic
367 ssDNA domains that can trigger downstream reactions such as transcription, hairpin chain reactions,[21] or
368 rolling circle amplification.[52] This expanded force range substantially broadens the design space for intelligent,

369 force-responsive material interfaces capable of cellular adaptation.

370 The all-nucleic-acid nature of aptamer MPs offers unique advantages by enabling seamless integration with
371 the broader toolbox of DNA nanotechnology. Without detaching MPs (or ligands), we introduced two modes
372 of precise upstream control over receptor engagement: Reversible switching via SDR and programmable timing
373 via RNase H–driven DRNs. Unlike protein- or nanobody-based MPs, this programmability requires no protein
374 engineering, expression, or purification, but only base-pairing logic. This molecular tunability allows
375 mechanotransduction to transcend simple linear outputs and adopt complex, nonlinear, and time-resolved
376 behaviors. Such temporal precision is especially vital in biological systems, such as morphogenesis and
377 embryonic development, where cells interpret mechanical and biochemical signals in tightly orchestrated
378 spatiotemporal patterns.[7]

379 Looking to the future, aptamer MPs could be further expanded by incorporating an upstream biochemical
380 control layer responsive to endogenous signals, ranging from small molecules (e.g., ions, ATP), to proteins
381 (e.g., cytokines), to even specific cell types.[53] Acting as a molecular bridge, aptamer MPs can transduce force
382 into the exposure of cryptic ssDNA sites, which in turn can initiate localized signal amplification, recruit
383 biomolecular effectors, modulate synthetic receptors, and ultimately trigger feedback-regulated mechanical
384 circuits within or across cells. We envision that such aptamer-based, programmable, and feedback-coupled
385 mechano-adaptive systems could accelerate the development of cell-autonomous behaviors, guide adaptive
386 morphogenetic processes, and provide a foundation for future advances in synthetic biology and tissue
387 engineering.

388 **Methods**

389 **Materials**

390 Hydrogen peroxide (35 %), sulfuric acid (95 %), (3-Aminopropyl)triethoxysilane (APTES), phosphate buffered
391 saline (PBS) and ethanol were purchased from Carl Roth. Biotin-PEG-NHS 5K (HE041023-5K) was purchased
392 from Biopharma. Cyclo[Arg-Gly-Asp-d-Phe-Lys(PEG-PEG-azide)] (RGD-3759-PI), and Cyclo[Arg-Gly-Asp-D-Phe-
393 Lys(Biotin)] (cRGD-Biotin, PCI-3895-PI) were purchased from Biosynth. 25 mm x 75 mm glass coverslips (10812),
394 and sticky slide 8 well (80828) were purchased from ibidi. All oligonucleotides were purchased from Biomers.
395 5-(N-ethyl-N-isopropyl) amiloride, chlorpromazine hydrochloride, Methyl-β-cyclodextrin, LY 294002,
396 Cytochalasin D and Blebbistati were purchased from Sigma-Aldrich. Streptavidin (434302), Alexa Fluor Plus 405
397 Phalloidin (A30104), CellTrace violet cell profileration kit (C34571), CellTrace far red cell proliferation kit
398 (C34564), bovine albumin fraction V (BSA, 7.5% solution), paraformaldehyde solution (4% in PBS),anti-PTK7
399 monoclonal antibody (MA5-25774), Alexa Fluor 488 anti-CD227 (Mucin-1) monoclonal antibody (53-9893-82),
400 Alexa Fluor 488 anti-CD326 (EpCAM) monoclonal antibody (53-8326-42), and Alexa Fluor 488 goat anti-mouse

401 IgG (H+L) cross-adsorbed secondary antibody (A-11001) were purchased from Thermo Fisher Scientific. RNase
402 H was purchased from New England Biolabs. Actin protein (>95% pure, rabbit skeletal muscle) was purchased
403 from Cytoskeleton, Inc. All buffers were prepared with nuclease free water. All chemicals and enzymes were
404 used as such without any further purification.

405 **DNA Hybridization**

406 DNA concentrations were determined using a DeNovix-S-06873 (DeNovix OS 0.8.1 v4.1.5) spectrophotometer.
407 DNA oligonucleotides were hybridized at 10 µM in a TE buffer additionally containing 12.5 mM $MgCl_2$ in 200
408 µL PCR tubes and subsequently diluted to 125 nM. DNA oligonucleotides were heated to 95 °C and then cooled
409 at a rate of 1.3 °C/min to 25 °C.

410 **Surface preparation**

411 Surface preparation method was modified from previously published protocols.[21] Briefly, glass coverslips (25 x
412 75 mm) were rinsed with ultrapure water and sequentially sonicated in water and ethanol for 20 min each.
413 The coverslips were then immersed in freshly prepared piranha solution (3:1 v/v concentrated sulfuric acid
414 (95 %) to hydrogen peroxide (30 %)) for 1 h. **Caution:** Piranha solution becomes very hot upon mixing, and is
415 highly oxidizing and may explode upon contact with organic solvents. Then, the coverslips were washed 6 times
416 with ultrapure water, followed by 4 successive ethanol washes. For amine functionalization, the coverslips were
417 incubated in 3 % v/v APTES at room temperature for 1 h. The coverslips were then washed 6 times with ethanol,
418 and baked at 80 °C for 20 min. Slides were then reacted with Biotin-PEG-NHS (1 % w/v) for 1 h in ultrapure
419 water. Next, the coverslips were washed 3 times with ultrapure water, dried under N_2 gas, and stored at -80°C
420 until use.

421 The biotinylated coverslips were adhered to sticky-slide 8-well chambers. Wells were incubated with 50 µg/mL
422 of streptavidin for 1 h at room temperature, followed by three washes with nuclease-free water. Wells were
423 then incubated with 200 µL of 250 nM probe solution (125 nM cRGD-biotin and 125 nM DNA probes) for 1 h
424 at room temperature. After washing with nuclease free water, cell imaging media (1 % FBS, 1 % P/S, DMEM;
425 see below) was added to the well followed by the addition of cells.

426 **Cell culture and transfection**

427 HeLa (ACC 57) and HepG2 (ACC 180) were purchased from DSMZ. A549 (DSMZ, ACC 107) and MDA-MB-231
428 (DSMZ, ACC 732) were gifts from Tanja Weil laboratory at Max Planck Institute for Polymer Research. HeLa cells
429 were cultured in Minimum Essential Medium (MEM) (10 % fetal bovine serum (FBS), 1 % penicillin–
430 streptomycin (P/S)) at 37 °C with 5 % CO_2. A549 and MDA-MB-231 cells were cultured in Dulbecco's Modified
431 Eagle Medium (DMEM) (10 % FBS, 1 % P/S) at 37 °C with 5 % CO_2. HepG2 cells were cultured in RPMI 1640

432 Medium (10 % FBS, 1 % P/S) at 37 °C with 5 % CO_2. mEGFP-paxillin WT plasmid was a gift from Michael Rosen
433 (Addgene plasmid # 186152).[54] Transfection was carried out using the Lipofectamine 3000 Transfection
434 Reagent (Invitrogen, L3000015) following the manufacturer's instructions.

435 **Force imaging, image acquisition and analysis**

436 All cells were seeded onto the MP surfaces in cell imaging medium (1% FBS, 1% P/S, DMEM) and incubated at
437 37 °C with 5 % CO2 for 4 h, except for Figs. 6h-i, where incubation times were 2, 4, and 7 h. TIRF and brightfield
438 microscopy were performed on a Zeiss Elyra 7 Imaging System equipped with 405 nm, 488 nm, 561 nm, and
439 642 nm excitation lasers using alpha Plan-Apochromat 63x, N.A. 1.46.oil immersion, TIRF objective, pco.edge
440 4.2 CLHS water-cooled sCMOS cameras. Live cell imaging was conducted at 37 °C in humidified air with 5 %
441 CO_2. Microscopy experiments were typically conducted using the following parameters: 405 nm laser: 0.4 %
442 output (~0.01 mW), 488 nm laser: 0.8 % output (~0.7 mW), 561 nm laser: 0.8 % output (~0.8 mW) and 642 nm
443 laser: 0.4 % output (~0.4 mW). Beam splitters (primary, secondary): LBF 405/488/561/642, SBS BP 490-560 +
444 LP 640. Exposure time: 50 ms (except for Fig. 2d, RRX-AS1411 200 ms, Atto488-TB-5 200 ms; Fig. 5h, A549-
445 Violet 200 ms; Fig. 5j, HeLa-Deep Red 100 ms, HepG2-Violet 200 ms). TIRF angle: 66° (n_{oil}: 1.518). All images
446 were contrasted equally.

447 Background subtraction methods were adapted from previously published protocols.[55] Briefly raw images were
448 exported to FIJI (software) followed by selecting 3 ROIs in the fluorescent channel, next the background
449 intensity was measured and subtracted from the images.

450 **Inhibition experiments**

451 100 µM 5-(N-ethyl-N-isopropyl) amiloride (EIPA), 1.9 µM Methyl-β-cyclodextrin (MβCD), 28 µM
452 chlorpromazine hydrochloride (CPZ) were used to inhibit the macropinocytosis, caveolae and clathrin-
453 mediated internalization, respectively. 50 µM LY 294002 was used to inhibit the PI3K. 10 µM cytochalasin D
454 and 25 µM Blebbistatin were used to inhibit the actin polymerization and myosin ATPase, respectively.

455 **Immunostaining**

456 Cells were fixed with 4 % (w/v) paraformaldehyde in PBS for 15 min at room temperature and permeabilized
457 with 0.25 % (v/v) Triton X-100 in PBS for 10 min, followed by washes in PBS twice. Unspecific binding was
458 blocked using 10 % normal goat serum in PBS for 30 min at room temperature. After removing blocking solution,
459 cells were incubated with Alexa Fluo Plus 405 Phalloidin (1:200 dilution) in 2.5 % (w/v) BSA/PBS at room
460 temperature for 1 h. Samples were then washed three times in PBS for 5 min each before microscopic
461 observations.

462 **Flow cytometry**

463 To assess the competitive binding of endostatin to nucleolin, 5×10^5 cells were incubated with 25 μg/mL
464 endostatin and 2.5 μM FAM-AS1411 in 3 % (w/v) BSA/PBS at 4 °C for 60 min. Cells were washed and then
465 resuspended in PBS before running through flow cytometer. To quantify the receptor expression levels, 5×10^5
466 cells were labelled with fluorescent primary antibodies (Alexa Fluor™ 488-anti-MUC1: 5 μg/mL, Alexa Fluor™
467 488-anti-EpCAM: 5 μg/mL) in 3 % (w/v) BSA/PBS at 4 °C for 30 min. For labelling PTK7, cells were incubated
468 with primary antibody anti-PTK7 (2 μg/mL) in 3 % (w/v) BSA/PBS at 4 °C for 30 min. Cells were washed three
469 times with PBS and then incubated in Alexa Fluor™ 488-secondary antibody (5 μg/mL) in 3 % (w/v) BSA/PBS at
470 37 °C for 30 min. After labelling, cells were washed and resuspended in PBS. To assess the effect of EIPA on
471 AS1411 internalization, 2×10^5 cells were seeded in standard cell medium in 12-well plates and incubated
472 overnight at 37 °C. Cells were then incubated with 100 μM EIPA and 500 nM FAM-AS1411 in 1 % FBS/DMEM
473 at 37 °C for 4 h. Cells were washed and then resuspended in PBS before running through flow cytometer.

474 Flow cytometry experiments were performed on a Novocyte Quanteon (Agilent, NovoExpress v.1.6.0) with 4
475 excitation lasers (violet 405 nm, blue 488 nm, yellow-green 561 nm and red 640 nm) and 16 fluorescence
476 detectors. A total of 10,000 events were collected per sample. Flow cytometry data was analyzed using
477 FLOWJO (v10.8.1) software.

478 **Statistical analysis**

479 Each experiment was performed at least three independent times. Statistical results were analyzed using
480 GraphPad Prism 8.0 and shown as the mean ± s.d. Comparisons between two groups were conducted using
481 unpaired two-tailed Student's *t*-test (Figs. 4m and 5i), and among three or more groups using one-way ANOVA
482 with Bonferroni test correction (Figs. 4h and 6c) as indicated. If a data set did not pass the normality tests, the
483 significances were calculated with Mann-Whitney (Figs. 2e, 5b, 5d, 5f and 5k) for two-group comparisons or
484 Kruskal-Wallis corrected with Dunn's test (Figs. 2b-c, 3c-e, 4b and 4f) for multiple groups. Comparisons of time
485 course changes in fluorescence intensity of HeLa cells on RNA-blocked AS1411 MP surfaces after adding 10
486 U/mL RNase H and varying RNA/DNA duplex concentrations were performed using two-way ANOVA with
487 Geisser-Greenhouse correction followed by Bonferroni post-hoc tests (Figs. 6h,i). For all analyses, $^*P < 0.05$,
488 $^{**}P < 0.01$ and $^{***}P < 0.001$, $^{****}P < 0.0001$ were considered significant. NS indicates statistical non-
489 significance with $P > 0.05$.

490 **Acknowledgments**

491 We would like to thank Dr. Siyu Song and Dr. Miao Xie for their helpful discussion about cell experiments. We
492 acknowledge IMB Flow Cytometry Core Facility for the flow cytometry data acquisition. This project has
493 received funding from the European Research Council (ERC) under the European Union's Horizon 2020
494 research and innovation program (M3ALI:101001638), as well as from the CoM2Life start-up funds of JGU.

T. X. acknowledges support from the Max Planck Graduate Center. A. W. acknowledges funding via a Gutenberg Research Professorship and a Max Planck Fellowship underpinning his Life-Like Materials Program. The Zeiss Elyra 7 was funded by the Gutenberg Research College and Deutsche Forschungsgemeinschaft (DFG; 497845157). Open Access funding enabled and organized by Projekt DEAL.

Author Contributions

T.X. and A.W. conceived the project. T.X. designed, performed all the experiments, and conducted data analysis. S.S. helped with the surface preparation and probe immobilization. C.D. helped with TIRF measurement. T.X., S.S. C.D. and A.W. discussed the data. T.X. and A.W. wrote the manuscript with input from all authors. A.W. supervised the project.

Competing interests

The authors declare no conflict of interest.

Data availability

All data are available in the article and its Supplementary Information are available from the corresponding author upon reasonable request.

Supplementary Information

Supplementary information is available in the online version of the paper.

Reference

1. Vining, K. H. & Mooney, D. J. Mechanical forces direct stem cell behaviour in development and regeneration. *Nat. Rev. Mol. Cell Biol.* **18**, 728–742 (2017).
2. Iskratsch, T., Wolfenson, H. & Sheetz, M. P. Appreciating force and shape — the rise of mechanotransduction in cell biology. *Nat. Rev. Mol. Cell Biol.* **15**, 825–833 (2014).
3. Van Helvert, S., Storm, C. & Friedl, P. Mechanoreciprocity in cell migration. *Nat. Cell. Biol.* **20**, 8–20 (2018).
4. Chaudhuri, O., Cooper-White, J., Janmey, P. A., Mooney, D. J. & Shenoy, V. B. Effects of extracellular matrix viscoelasticity on cellular behaviour. *Nature* **584**, 535–546 (2020).
5. Huebsch, N. *et al.* Harnessing traction-mediated manipulation of the cell/matrix interface to control stem-cell fate. *Nat. Mater.* **9**, 518–526 (2010).
6. Kim, S., Uroz, M., Bays, J. L. & Chen, C. S. Harnessing Mechanobiology for Tissue Engineering. *Dev. Cell* **56**, 180–191 (2021).
7. Negrete, J. & Oates, A. C. Towards a physical understanding of developmental patterning. *Nat. Rev. Genet.* **22**, 518–531 (2021).
8. Toettcher, J. E., Voigt, C. A., Weiner, O. D. & Lim, W. A. The promise of optogenetics in cell biology: interrogating molecular circuits in space and time. *Nat. Methods* **8**, 35–38 (2011).
9. Seo, D. *et al.* A Mechanogenetic Toolkit for Interrogating Cell Signaling in Space and Time. *Cell* **165**, 1507–1518 (2016).
10. Kechagia, J. Z., Ivaska, J. & Roca-Cusachs, P. Integrins as biomechanical sensors of the microenvironment. *Nat. Rev. Mol. Cell Biol.* **20**, 457–473 (2019).
11. De Belly, H., Paluch, E. K. & Chalut, K. J. Interplay between mechanics and signalling in regulating cell fate.

Nat. Rev. Mol. Cell Biol. **23**, 465–480 (2022).
12. Hu, Y. *et al.* Quantifying T cell receptor mechanics at membrane junctions using DNA origami tension sensors. *Nat. Nanotechnol.* **19**, 1674–1685 (2024).
13. Xiao, B. Mechanisms of mechanotransduction and physiological roles of PIEZO channels. *Nat. Rev. Mol. Cell Biol.* **25**, 886–903 (2024).
14. Wang, X. & Ha, T. Defining Single Molecular Forces Required to Activate Integrin and Notch Signaling. *Science* **340**, 991–994 (2013).
15. Hu, Y., Duan, Y. & Salaita, K. DNA Nanotechnology for Investigating Mechanical Signaling in the Immune System. *Angew. Chem. Int. Ed.* **62**, e202302967 (2023).
16. Jo, M. H. *et al.* Determination of single-molecule loading rate during mechanotransduction in cell adhesion. *Science* **383**, 1374–1379 (2024).
17. Hu, Y. *et al.* DNA-based ForceChrono probes for deciphering single-molecule force dynamics in living cells. *Cell* **187**, 3445-3459.e15 (2024).
18. Slack, R. J., Macdonald, S. J. F., Roper, J. A., Jenkins, R. G. & Hatley, R. J. D. Emerging therapeutic opportunities for integrin inhibitors. *Nat. Rev. Drug Discov.* **21**, 60–78 (2022).
19. Pawlak, M. R. *et al.* RAD-TGTs: high-throughput measurement of cellular mechanotype via rupture and delivery of DNA tension probes. *Nat. Commun.* **14**, 2468 (2023).
20. Yang, S. *et al.* DNA-functionalized artificial mechanoreceptor for de novo force-responsive signaling. *Nat. Chem. Biol.* **20**, 1066–1077 (2024).
21. Duan, Y. *et al.* Mechanically Triggered Hybridization Chain Reaction. *Angew. Chem. Int. Ed.* **60**, 19974–19981 (2021).
22. Morsut, L. *et al.* Engineering Customized Cell Sensing and Response Behaviors Using Synthetic Notch Receptors. *Cell* **164**, 780–791 (2016).
23. Langridge, P. D. & Struhl, G. Epsin-Dependent Ligand Endocytosis Activates Notch by Force. *Cell* **171**, 1383-1396.e12 (2017).
24. Stabley, D. R., Jurchenko, C., Marshall, S. S. & Salaita, K. S. Visualizing mechanical tension across membrane receptors with a fluorescent sensor. *Nat. Methods* **9**, 64–67 (2012).
25. Sun, M., Deng, J. & Walther, A. Communication and Cross-Regulation between Chemically Fueled Sender and Receiver Reaction Networks. *Angew. Chem. Int. Ed.* **62**, e202214499 (2023).
26. Deng, J. & Walther, A. Autonomous DNA nanostructures instructed by hierarchically concatenated chemical reaction networks. *Nat. Commun.* **12**, 5132 (2021).
27. Sharma, C., Samanta, A., Schmidt, R. S. & Walther, A. DNA-Based Signaling Networks for Transient Colloidal Co-Assemblies. *J. Am. Chem. Soc.* **145**, 17819–17830 (2023).
28. Ma, Y. *et al.* Advancing targeted combination chemotherapy in triple negative breast cancer: nucleolin aptamer-mediated controlled drug release. *J. Transl. Med.* **22**, 604 (2024).
29. Choo, P., Liu, T. & Odom, T. W. Nanoparticle Shape Determines Dynamics of Targeting Nanoconstructs on Cell Membranes. *J. Am. Chem. Soc.* **143**, 4550–4555 (2021).
30. Liu, Y. *et al.* A Non-G-Quadruplex DNA Aptamer Targeting NCL for Diagnosis and Therapy in Bladder Cancer. *Adv. Healthc. Mater.* **12**, 2300791 (2023).
31. Jurchenko, C., Chang, Y., Narui, Y., Zhang, Y. & Salaita, K. S. Integrin-Generated Forces Lead to Streptavidin-Biotin Unbinding in Cellular Adhesions. *Biophys. J.* **106**, 1436–1446 (2014).
32. Jo, M. H. *et al.* Single-molecule characterization of subtype-specific β1 integrin mechanics. *Nat. Commun.* **13**, 7471 (2022).
33. Yin, J. *et al.* An intelligent DNA nanodevice for precision thrombolysis. *Nat. Mater.* **23**, 854–862 (2024).
34. Velusamy, A., Sharma, R., Rashid, S. A., Ogasawara, H. & Salaita, K. DNA mechanocapsules for programmable piconewton responsive drug delivery. *Nat. Commun.* **15**, 704 (2024).
35. Li, S. *et al.* A DNA nanorobot functions as a cancer therapeutic in response to a molecular trigger in vivo. *Nat. Biotechnol.* **36**, 258–264 (2018).
36. Di, Z. *et al.* An orthogonally regulatable DNA nanodevice for spatiotemporally controlled biorecognition and tumor treatment. *Sci. Adv.* **6**, eaba9381 (2020).
37. Tang, H. *et al.* Cholesterol modulates the physiological response to nanoparticles by changing the

583 composition of protein corona. *Nat. Nanotechnol.* **18**, 1067–1077 (2023).
584 38. Wang, Z. *et al.* Organelle-Specific Triggered Release of Immunostimulatory Oligonucleotides from
585 Intrinsically Coordinated DNA–Metal–Organic Frameworks with Soluble Exoskeleton. *J. Am. Chem. Soc.*
586 **139**, 15784–15791 (2017).
587 39. Commisso, C. *et al.* Macropinocytosis of protein is an amino acid supply route in Ras-transformed cells.
588 *Nature* **497**, 633–637 (2013).
589 40. Kotula, J. W. *et al.* Aptamer-Mediated Delivery of Splice-Switching Oligonucleotides to the Nuclei of Cancer
590 Cells. *Nucl. Acid Ther.* **22**, 187–195 (2012).
591 41. Ding, Y. *et al.* Heat Shock Cognate 70 Regulates the Translocation and Angiogenic Function of Nucleolin.
592 *Arterioscler. Thromb. Vasc. Biol.* **32**, e126–e134 (2012).
593 42. Kechagia, Z. *et al.* The laminin–keratin link shields the nucleus from mechanical deformation and signalling.
594 *Nat. Mater.* **22**, 1409–1420 (2023).
595 43. Rennick, J. J., Johnston, A. P. R. & Parton, R. G. Key principles and methods for studying the endocytosis of
596 biological and nanoparticle therapeutics. *Nat. Nanotechnol.* **16**, 266–276 (2021).
597 44. Schink, K. O. *et al.* The phosphoinositide coincidence detector Phafin2 promotes macropinocytosis by
598 coordinating actin organisation at forming macropinosomes. *Nat. Commun.* **12**, 6577 (2021).
599 45. Mercer, J. & Helenius, A. Virus entry by macropinocytosis. *Nat. Cell Biol.* **11**, 510–520 (2009).
600 46. Swanson, J. A. Shaping cups into phagosomes and macropinosomes. *Nat. Rev. Mol. Cell Biol.* **9**, 639–649
601 (2008).
602 47. Quinn, S. E. *et al.* The structural dynamics of macropinosome formation and PI3-kinase-mediated sealing
603 revealed by lattice light sheet microscopy. *Nat. Commun.* **12**, 4838 (2021).
604 48. Du, Y. *et al.* Ligand Dilution Analysis Facilitates Aptamer Binding Characterization at the Single-Molecule
605 Level. *Angew. Chem. Int. Ed.* **135**, e202215387 (2023).
606 49. Ferreira, C. S. M., Matthews, C. S. & Missailidis, S. DNA Aptamers That Bind to MUC1 Tumour Marker:
607 Design and Characterization of MUC1-Binding Single-Stranded DNA Aptamers. *Tumor Biol.* **27**, 289–301
608 (2006).
609 50. Song, Y. *et al.* Selection of DNA Aptamers against Epithelial Cell Adhesion Molecule for Cancer Cell Imaging
610 and Circulating Tumor Cell Capture. *Anal. Chem.* **85**, 4141–4149 (2013).
611 51. Singuru, M. M. R., Amouzadeh Tabrizi, M., Bhattacharyya, P., Ali, A. A. & You, M. Force-Responsive Delivery
612 of Anticancer Drugs via a DNA Mechanical Nanovehicle. *Nano Lett.* **25**, 336–342 (2025).
613 52. Ma, V. P. *et al.* Mechanically Induced Catalytic Amplification Reaction for Readout of Receptor-Mediated
614 Cellular Forces. *Angew. Chem. Int. Ed.* **128**, 5578–5582 (2016).
615 53. Samanta, A., Baranda Pellejero, L., Masukawa, M. & Walther, A. DNA-empowered synthetic cells as
616 minimalistic life forms. *Nat. Rev. Chem.* **8**, 454–470 (2024).
617 54. Case, L. B., De Pasquale, M., Henry, L. & Rosen, M. K. Synergistic phase separation of two pathways
618 promotes integrin clustering and nascent adhesion formation. *eLife* **11**, e72588 (2022).
619 55. Sethi, S. *et al.* Nuclease-Resistant L-DNA Tension Probes Enable Long-Term Force Mapping of Single Cells
620 and Cell Consortia. *Angew. Chem. Int. Ed.* **63**, e202413983 (2024).
621